
# Highly Stable Fe3O4/C Composite: A Candidate Material for All Solid-State Lithium-Ion Batteries

Journal of The Electrochemical Society

The Electrochemical Society
Advancing solid state & electrochemical science & technology

OPEN ACCESS

# Highly Stable $Fe_3O_4$/C Composite: A Candidate Material for All Solid-State Lithium-Ion Batteries

To cite this article: F. Maroni *et al* 2020 *J. Electrochem. Soc.* **167** 070556

*Journal of The Electrochemical Society*, 2020 **167** 070556

# Highly Stable $Fe_3O_4$/C Composite: A Candidate Material for All Solid-State Lithium-Ion Batteries

**F. Maroni,[1] P. Bruni,[1] N. Suzuki,[2] Y. Aihara,[2,*] S. Gabrielli,[3] G. Carbonari,[3] M. Agostini,[4] M. Branchi,[5] S. Ferrari,[1] M. A. Navarra,[5] S. Brutti,[5] A. Matic,[4] F. Nobili,[3] and F. Croce[1,*,z]**

[1]*Dipartimento di Farmacia, Università "G. D'Annunzio" Chieti-Pescara, I-66100 Chieti, Italy*
[2]*Samsung R&D Institute Japan, Minoh-shi, Osaka 562-0036, Japan*
[3]*Scuola di Scienze e Tecnologie—Università di Camerino, I-62032 Camerino (MC), Italy*
[4]*Department of Physics, Chalmers University of Technology, SE-41296 Göteborg, Sweden*
[5]*Dipartimento di Chimica, Università di Roma "La Sapienza", P.le Aldo Moro, 00185 Roma, Italy*

$Fe_3O_4$ nanoparticles synthesized by a base catalyzed method are tested in an All-Solid-State (ASLB) battery using a sulfide electrolyte. The pristine nanoparticles were morphologically characterized showing an average size of 12 nm. The evaluation of the electrochemical properties shows high specific capacity values of 506 $mAhg^{-1}$ after 350 cycles at a specific current of 250 $mAg^{-1}$, with very high stability and coulombic efficiency.
 [DOI: 10.1149/1945-7111/ab80ce]

Manuscript submitted December 25, 2019; revised manuscript received March 12, 2020. Published April 8, 2020. *This paper is part of the JES Focus Issue on Challenges in Novel Electrolytes, Organic Materials, and Innovative Chemistries for Batteries in Honor of Michel Armand.*

Supplementary material for this article is available online

The large development of Li-ion technology allows for a massive spreading of portable electronics, as well as for a progressive diffusion of electrical vehicles (EV). However, the increasing demand for battery systems with higher energy density requests a breakthrough in finding new materials.[1] In the last decade, the industry standard has been represented by insertion materials for both anode and cathode, while recently alloy-forming materials with $Li_xZ$ (Z = Si, Sn, Sb, Bi) formula[2] have emerged as viable, alternative anodes materials. In addition, recently a new chemistry has surfaced, allowing to store more $Li^+$ by the so-called conversion mechanism.[3–5] In this process the active material is reversibly reduced into metallic nanoclusters embedded in a $Li_2O$ matrix,[6,7] following the general Eq. 1:

$$M_xO_y + 2ye^- + 2yLi^+ \leftrightarrow xM^0 + yLi_2O \quad [1]$$

Among the others, several transition metal oxides,[8] sulfides,[9] nitrides,[10] phosphides[11] and fluorides[12] have been explored and tested as conversion anodes. Considering 3d-transition metal oxides, among iron oxides $\alpha$-$Fe_2O_3$ and $Fe_3O_4$ have received great attention.[13]

$Fe_3O_4$, also known as magnetite, is a low cost, environmentally benign metal oxide that can undertake a reversible conversion reaction with $Li^+$ ions,[14] according to Eq. 2 which results in a theoretical capacity of 924 $mAhg^{-1}$, almost 3 times higher than the commercially available graphite anode:

$$Fe_3O_4 + 8e^- + 8Li^+ \leftrightarrow 3Fe^0 + 4Li_2O \quad [2]$$

Despite these premises, transition metal oxides associated with the conversion mechanism usually suffer from a series of issues intimately connected with the conversion reaction itself. In fact, remarkable structural changes and volume expansion are associated with this mechanism,[6] eventually leading to pulverization and loss of contact between active material particles and the current collector, which result in poor electron and ion transport limiting the overall cycle-life.

In order to improve the electrochemical performance, different approaches have been proposed: firstly, the use of composite nanoarchitectures with optimized morphologies, such as nanorods,[15] hollow[16] or nano-spheres[17] and carbon coating strategies[18–20]; lastly the use of graphene to form composites[21–23] showed remarkable improvements in terms of cycle-life.

Here, we report the synthesis, characterization and evaluation of the electrochemical properties of pristine $Fe_3O_4$ nanoparticles synthesized from a base catalyzed method mechanically mixed with electrospun Polyacrylonitrile (PAN) derived carbon fibers as simple composite material. The $Fe_3O_4$/C electrodes are characterized by galvanostatic cycling experiments using currents as high as 2000 mA $g^{-1}$, revealing high capacity values and capacity retention, together with a very good capacity recovery during the rate capability experiment.

## Experimental

***$Fe_3O_4$ nanoparticle synthesis and characterization.***—$Fe_3O_4$ nanoparticles were synthesized using a previously reported method[24]: 1.0 g of $FeCl_2{\cdot}4H_2O$ and 2.7 g of $FeCl_3{\cdot}6H_2O$ were dissolved in 20 ml of distilled $H_2O$ each, in two separate containers. The solutions were then mixed, and 100 ml of a 1.5 M solution of $NH_4OH$ were added at room temperature. Finally, 30 ml of a 25% w/w solution of $NH_4OH$ were added to the reaction mixture. The resulting dispersion was kept under reflux for 18 h and cooled down to room temperature. The resulting nanoparticles were recovered, rinsed three times with distilled $H_2O$ and ethanol, and finally dried under vacuum at 50 °C.

The micro-nanofibers carbon mats were prepared through an electrospinning process. The polymer blend was prepared dissolving Polyacrylonitrile (Mw = 150000, Aldrich) in N,N-dimethylformamide (DMF, Aldrich). The solution was stirred for 20 h at 60 °C on a heating plate. The solution was electrospun at constant flow rate of 0.60 ml $h^{-1}$ and with a DC voltage of 15–18 kV. Relative humidity and environmental temperature were 20% and 30 °C, respectively. The needle was placed at 15 cm distance from the plate collector (covered with an aluminum foil), at 10° of inclination angle. Electrospun mats were thermally treated, under air flow, with a heating rate of 5 °C $min^{-1}$, at 250 °C for 1 h. Thermal reduction was performed at 700 °C under Ar:$H_2$ flow (95:5, 200 ml $min^{-1}$) at a

*Electrochemical Society Member.
[z]E-mail: fausto.croce@unich.it

heating rate of 10 °C $min^{-1}$ to 400 °C and then 5 °C $min^{-1}$ to 700 °C with a final plateau of 3 h. The $Fe_3O_4$/C composite was then prepared by directly ball-milling iron oxide particles and the PAN derived carbon nanofibers at 250 rpm for 1 h, using $ZrO_2$ spheres and a Retsch PM100 instrument. The $Fe_3O_4$:C ratio was 80:20.

The $Fe_3O_4$/C powder was characterized by means of X-ray diffraction (XRD) using a Rigaku Ultima diffractometer (Cu K$\alpha$ = 1.540 Å). X-ray photoelectron spectroscopy (XPS) data were acquired using a PHI 5800, Physical Electronics instrument, under Ar atmosphere, using Al K$\alpha$ radiation (200 W, 13 kV), at a pressure of $10^{-9}$ Torr. The diameter of the analyzed surface was 800 $\mu$m. The spectra were calibrated by the binding energy of the C 1s peak (BE = 284.5 eV). All spectra were fitted by the deconvolution software Casa XPS (Casa Software). Gaussian-Lorentzian (30% Gaussian) functions and a Shirley-type background were employed in all fitting spectra. SEM micrographs were recorded on a ZEISS LEO 1550 instrument, equipped with a X-MAXN EDX detector by Oxford Instruments. Transmission electron microscopy experiments have been carried out using a FEI Tecnai 200 kV cryo-TEM instrument. TEM pictures have been analyzed using the ImageJ software.[25] In particular simulated electron diffraction patterns have been reconstructed by performing a Fast-Fourier Transform (FFT) analysis of selected areas of the micrographs using the routines embedded in the ImageJ code. TEM samples have been prepared by suspending the powders in acetone by sonication: the suspension has been dropped on holey carbon grids and directly transferred into the microscope. Thermogravimetric analysis (TGA) has been performed with a Mettler-Toledo TGA/SDTA 851 instrument, in air atmosphere, in a temperature range of 25 °C–900 °C with a heating ramp of 10 °C $min^{-1}$.

***Cell assembly and electrochemical tests.***—The electrode powder was prepared by ball milling the active material, the solid-state electrolyte and carbon nanofibers (CNF) as conductive additive, in the 35 (Nanocomposite): 60 (Solid Electrolyte): 5 (CNF) proportion, respectively, at 250 rpm for 10 min. Solid state torque cells were assembled in Ar-filled glovebox (MBraun): 200 mg of a LiI:$Li_2S$-$P_2S_5$ solid state electrolyte were weighed and cold-pressed at 1 ton to prepare a pellet, then 5 mg of electrode powder (1.75 mg in $Fe_3O_4$/C content and 1.4 mg in pure $Fe_3O_4$) were weighed and put, with a Li-In counter electrode, into the respective side of the solid state cell and pressed at 4 ton. The cell was tightened using a torque wrench. Active material mass loading was 1.33 mg·$cm^{-2}$. Cyclic voltammetry, galvanostatic cycling tests and impedance experiments were performed using a VMP2/Z potentiostat/galvanostat (Bio-Logic) in the potential ranges 0.100 V–3.000 V. Impedance spectra were recorded with bias potential of E = 3.000 V, in the frequency range of 100 KHz–100 mHz with an oscillation amplitude of ±5 mV. Potential values were reported vs $Li^+$/Li couple. The electrochemical experiments were conducted at 40 °C in a Tenney TJR environmental chamber. Specific capacity values given in this paper are referred to the total $Fe_3O_4$/C content in the electrode powder mix.

## Results and Discussion

***Structural and morphological characterization.***—The $Fe_3O_4$/C composite was characterized using different techniques. Figure 1 reports the thermogravimetric analysis (TGA) and the X-ray Diffraction (XRD) spectra. Thermogravimetric analysis, Fig. 1a, shows a small weight loss, around 5%, up to 100 °C, due to volatile species and moisture residues in the sample. The progressive weight decrease, leading to a sharp loss at 400 °C, due to the conversion of carbon materials to $CO_2$, accounts for a total of 25% weight loss, which excluding moisture at the beginning, is in line with the $Fe_3O_4$/C proportions of the prepared composite. It is worth noting that the composite powders were always dried at 120 °C for 12 h under vacuum before moving them into the glovebox to assemble the torque cells.

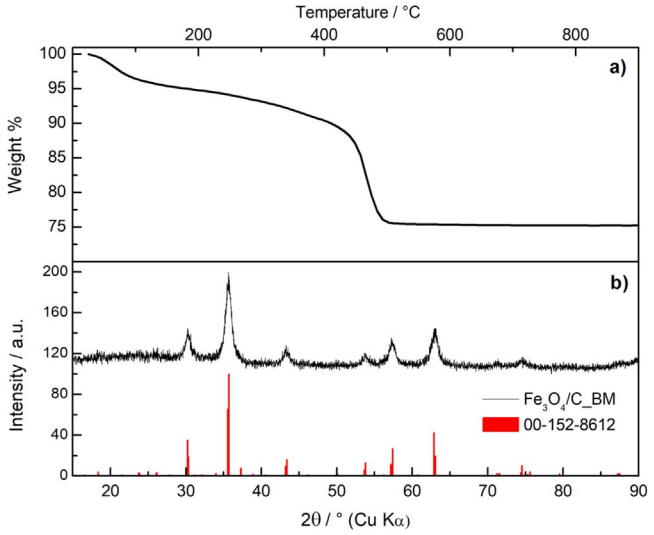


**Figure 1.** (a) Thermogravimetric analysis of the $Fe_3O_4$/C composite material (b) X-ray diffraction pattern of $Fe_3O_4$ nanoparticles, reference main peaks are indexed according to the Crystallography Open Database (COD) database.

The XRD pattern of the pristine magnetite powder, Fig. 1b, shows a series of peaks related to $Fe_3O_4$ diffraction (Crystallography Open Database (COD), card no. 00-152-8612). The small size of each crystallite is estimated as ~12.60 nm using Rietveld refinement (Maud software suite).[26] Rietveld data is shown in Table SI.

Figures 2a–2d reports the SEM images of pristine powder. The morphology of $Fe_3O_4$ is characterized by spherical shaped nanosized crystallites, aggregated in bigger secondary particles, without any peculiar feature. The electrospun polyacrylonitrile (PAN) derived carbon nanofibers are shorter than usual, due to the mechanical milling step during the preparation of the composite material. $Fe_3O_4$ nanoparticles result to be in close contact with the electrospun carbon fibers, thus the overall electronic conductivity is expected to be improved. Additional micrographs of the PAN-derived carbon nanofibers are reported in Fig. S1 (available online at stacks.iop.org/JES/167/070556/mmedia), detailing the difference in the pristine state, and after the ball milling.

The nanomorphology of the composite material has been investigated by TEM (see Figs. S2–S3) and conforms the observation by SEM. Despite the formation of aggregates, probably due to magnetic stirring during the synthetic procedure, the nanoparticles have a spherical shape with the boundaries of each single crystallite still visible, as can be seen in Fig. S1, reporting the HR-TEM micrographs. The large carbon matrixes are surrounded and decorated by dark nanoparticles, partially agglomerated. The FFT analysis of a selected area shown in the Fig. S3c is presented in the Fig. S3d. The simulated electron diffraction image confirms the identification of randomly oriented nanocrystals of magnetite $Fe_3O_4$, with cF56 structure.[27,28]

The crystallite size is evaluated in the range of 6 nm–13 nm (Fig. 1b), consistent with the value calculated by applying the Scherrer's equation.

X-ray photoelectron spectroscopy (XPS) analysis is performed to better understand the composition of the iron-based composite. The survey spectrum reported in Fig. 3a reveals the presence of Fe, O and C. The Fe 2p core level, Fig. 3b, shows different peaks which can be fitted with two spin–orbit doublets and a shakeup satellite. The doublets are related to the presence of $Fe^{3+}$ and $Fe^{2+}$. The results are consistent with the reported values for $Fe_3O_4$.[26,27] The O 1 s spectrum, Fig. 3c, is deconvoluted into two peaks, the main one at 530 eV is due to the presence of FeO species and can be attributed to $Fe_3O_4$ while the other peak at 531.1 eV is attributed to the presence of residual oxygen-containing groups in the sample

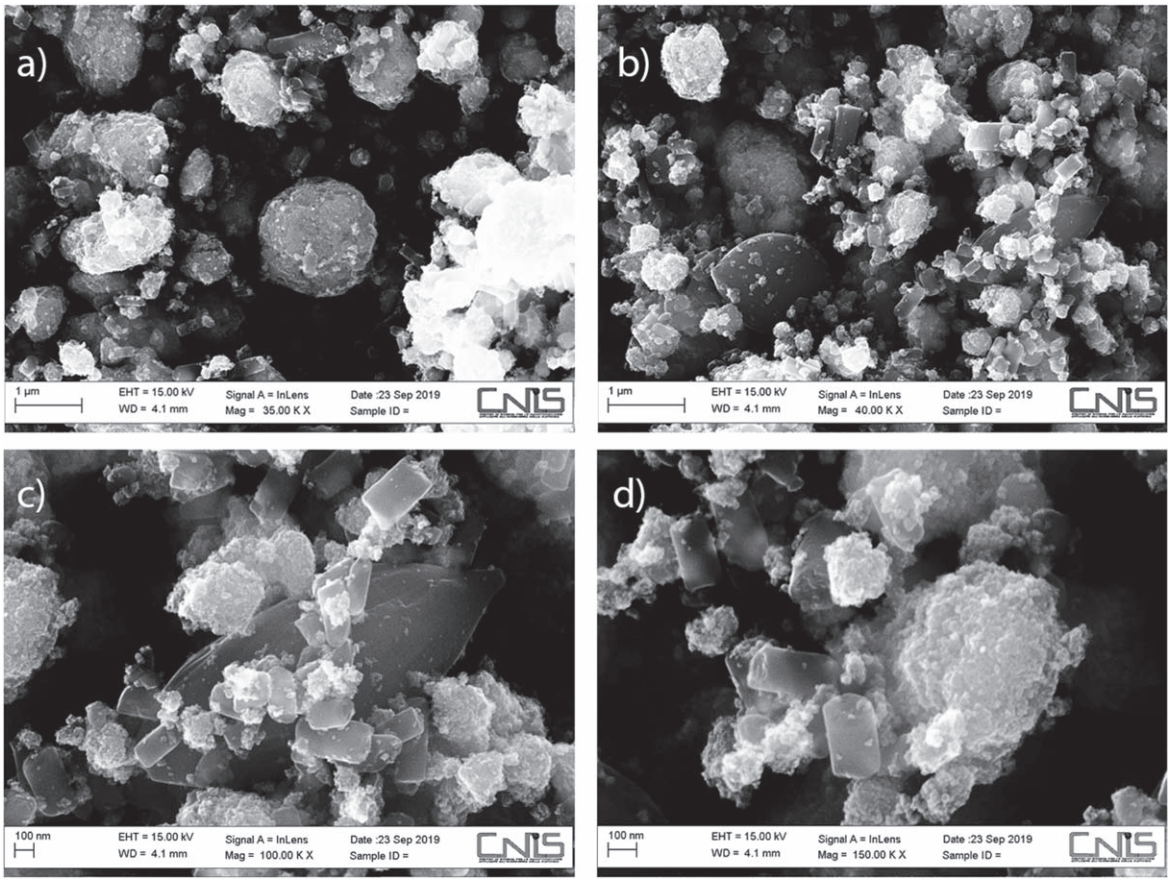


**Figure 2.** SEM micrograph of $Fe_3O_4$/C composite nanoparticles at different magnifications (a) 35 KX (b) 40KX (c) 100 KX (d) 150 KX.

(e.g. O–H etc…) which, in turn, could induce a small shift in the $Fe^{2+}$ and $Fe^{3+}$ related doublets.[29,30,31] The C1s core level, Fig. 3d, shows three peaks at 284.7, 286.2 and 289 eV related to C–C and C–O species as residual products from the synthesis of the electrode powder.[26,27]

***Electrochemical characterization.—***Electrochemical characterization using solid state electrolyte is performed by means of several techniques to have a wider picture on the cycling behavior and electrochemical performance. Cyclic voltammetry, Fig. 4, in the potential range 0.100 V–3.000 V at 0.050 $mVs^{-1}$ scan rate, evidences several electrochemical signals: during the first cathodic sweep, three peaks, at 1.66 V, 1.10 V and 0.70 V respectively, are visible. The peak at 1.66 V (indicated as * in Fig. 4) has been observed also by other authors: it describes a still not completely clear irreversible processes only occurring during first discharge.[32,33] The peak at 1.10 V (**A**) is consistent with the pre-lithiation of the iron oxide phase,[34] in which $Li^+$ ions are inserted into the spinel crystalline structure of $Fe_3O_4$ according to the reaction:

$$Fe_3O_4 + xLi^+ + xe^- \rightarrow Li_xFe_3O_4 \quad [3]$$

Then, the sharp peak at 0.70 V (**B**), describes the first-cycle reduction of the oxide nanoparticles to Fe metal[20,35] by the conversion reaction, leading to the formation of an amorphous composite of $Fe^0$ dispersed in a $Li_2O$ matrix.[4]

In the first anodic sweep a shoulder labeled as (**C**) is visible at E = 1.15 V, was assigned to $Li^+$ deinsertion from the PAN-derived carbon nanofibers, then a couple of broad and partially overlapped peaks are visible at 1.58 V and 1.82 V (**D**), which are attributed to the oxidation of the $Fe^0$ nanoparticles to $Fe^{2+}$ and $Fe^{3+}$, respectively. These results are consistent with literature data reported for liquid systems.[36,37] In the following cathodic sweep a pronounced hysteresis appears, following a well-known electrochemical behavior typical for conversion anode materials,[3] and the peak (**B**) shifts to 0.8 V, now labeled as peak (**D**). On the other hand, the anodic oxidation process, peak (**D**), remains substantially unchanged. From Cycle#2, another electrochemical process is activated at E = 2.45 V and was labeled as (**E**). It is of interest to investigate the presence of an additional reversible redox couple related to peak (**E**), visible in the successive voltammetry cycles, and labeled as peaks **F** and **G**, respectively, see Fig. S2.

Galvanostatic cycling were performed using a current of 250 mA $g^{-1}$ (current density 0.32 mA $cm^{-2}$) in the voltage range between 0.100 V < E < 3.000 V, the same used for the cyclic voltammetry experiment, to ensure both reproducibility and to limit $Li^+$ insertion into the PAN-derived carbon fibers at very low potentials.[38]

The obtained results are reported in Fig. 5. The panel (a) reports the prolonged cycling performance of the $Fe_3O_4$ nanoparticles highlighting a first discharge capacity of 1049 $mAhg^{-1}$ and a subsequent charge at 643 $mAhg^{-1}$, with coulombic efficiency around 61%. The first-cycle irreversible capacity is attributed to irreversible processes which could be associated to the formation of a passivation layer on the active material particles, as already evidenced by the CV experiment of Fig. 4. During the following 15 cycles, the capacity is stabilized at around 506 $mAhg^{-1}$ for the remaining 335 cycles, with coulombic efficiency steadily exceeding 99.5%.

The galvanostatic E vs Q profiles of the first discharge step, Fig. 5b, reveal two short sloping plateaus at 1.93 V and 1.65 V, a short sloping plateau at 1.02 V, and a larger one at 0.76 V. The profile associated with the subsequent charge step presents a sloping plateau which extends from 1.5 V to 1.90 V. The profiles are almost consistent with the cycling voltammetry experiment. From the second charge/discharge cycle, any sign of definite plateaus disappears in favor of a more sloped line around 1.0 V during the discharge steps, and from

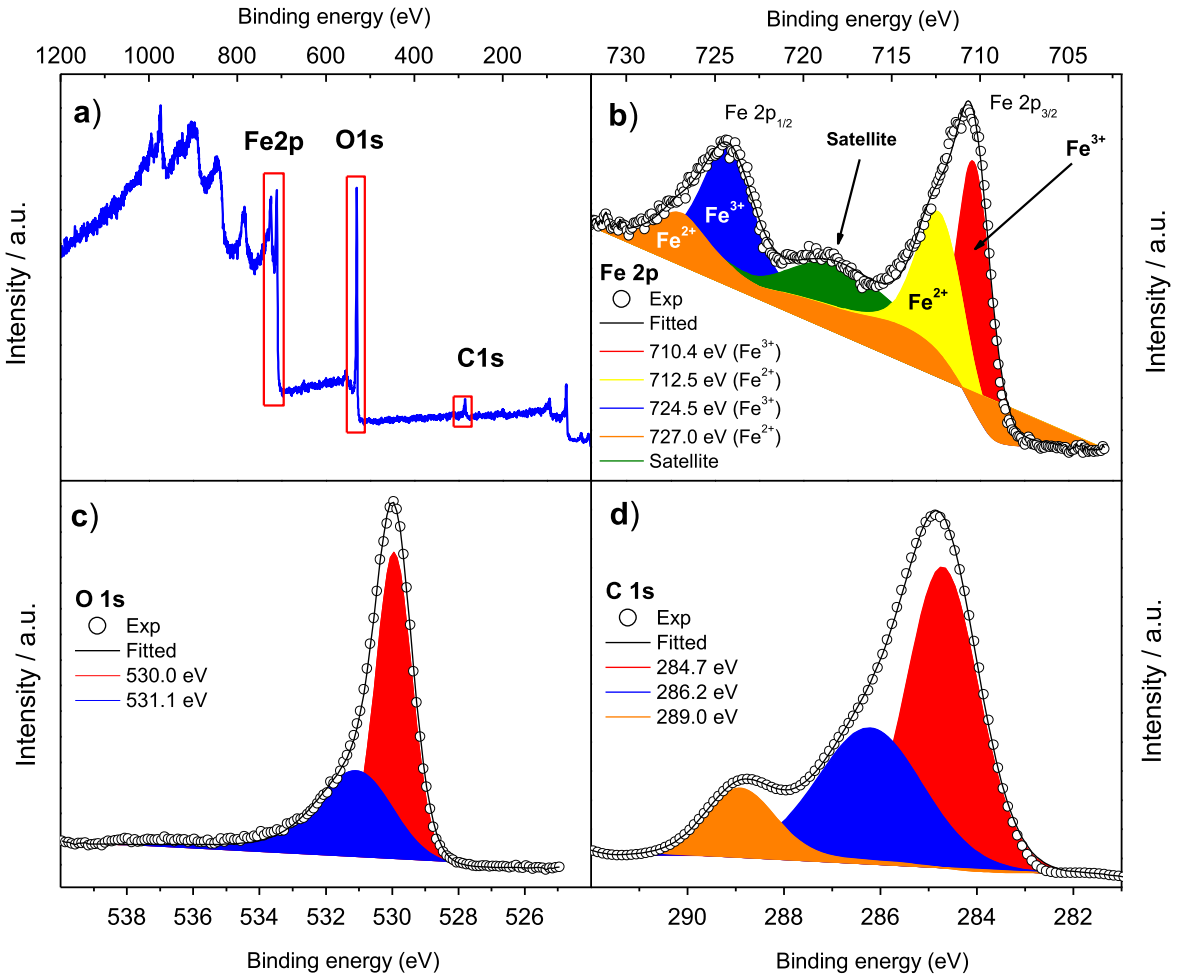


**Figure 3.** X-Ray Photoelectron Spectroscopy characterization of $Fe_3O_4$ composite material: (a) Survey spectrum (b) Experimental and fitted plot of the Fe2p core level. (c) Experimental and fitted plot of the O1s and (d) C1s core levels.

1.6 V to 1.75 V during the charge steps. Additionally, with increasing cycle number a reversible short sloping plateau is visible at 2.45 V, which is assigned to a broad potential interval in which can be present both the $Li_2S$ and the $Li_3PS_4$ electrochemical reactions.[39] Furthermore, the presence of a $Li_2S$ related peak, could be associated with some amorphous unreacted $Li_2S$, left over during the electrolyte ball-milling preparation step and introduced into the electrodic composite formulation mixture. This behavior has not been fully understood yet. The data showed in Fig. 5b, is even clearer in the differential plots shown in Fig. 5c, in which all the signals present in the cyclic voltammetry are present, showing a highly stable and reversible behavior up to cycle 300.

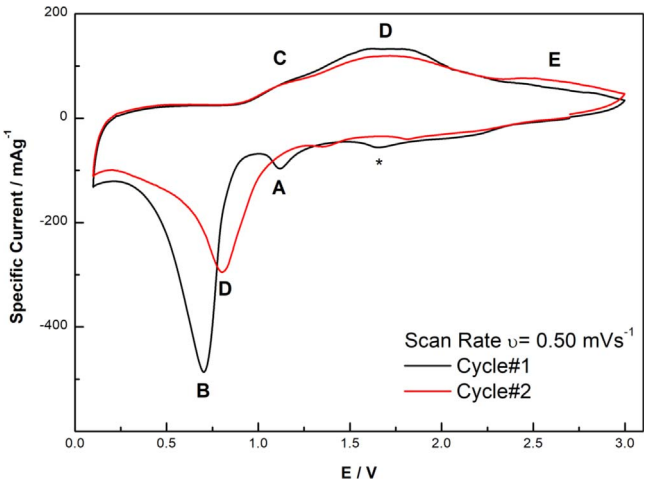


**Figure 4.** Cyclic Voltammetry of $Fe_3O_4$. Scan rate: 0.050 $mVs^{-1}$. Working potential range: 0.001 V < E < 3.000 V.

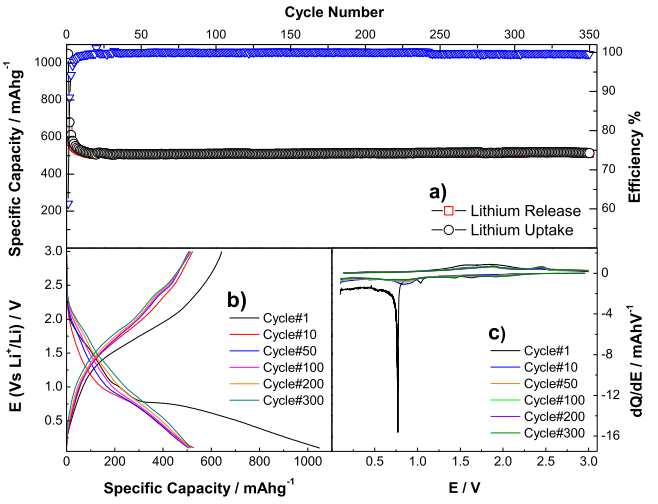


**Figure 5.** Cycling behavior of $Fe_3O_4$/PAN cell at 250 $mAg^{-1}$ specific current. 0.100 V < E < 3.000 V. (a) Charge/discharge capacity; (b) E vs Q profiles of selected cycles; (c) calculated dQ/dE differential plots.

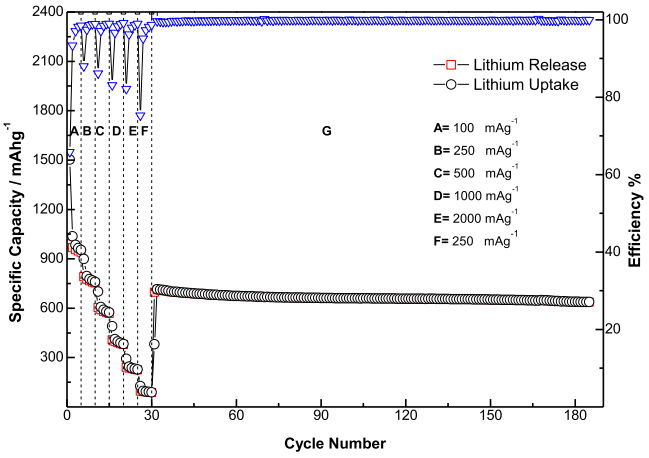


**Figure 6.** Rate capability experiment of $Fe_3O_4$/C electrodes in solid state configuration cell. Current rate from 100 to 2000 mA $g^{-1}$ and voltage range 0.100 V < E < 3.000 V.

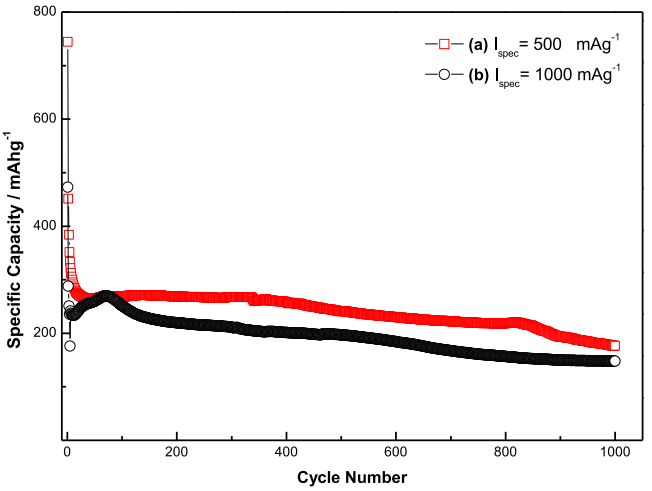


**Figure 7.** Extended galvanostatic performance of $Fe_3O_4$/C cells comparison; 0.100 V < E < 3.000 V (a) $I_{spec}$ = 500 mA $g^{-1}$; (b) $I_{spec}$ = 1000 mA $g^{-1}$.

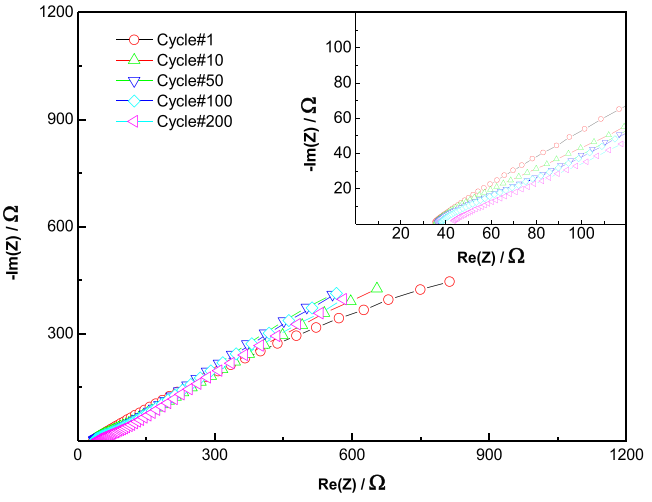


**Figure 8.** Nyquist plots of $Fe_3O_4$/C all-solid-state cell. Bias potential of 3.000 V, frequency range of 100 KHz < f < 100 mHz; Oscillation Amplitude ΔE = ±5 mV.

The large voltage hysteresis after the first discharge and visible changes in the shape of voltage profiles, are typical features of conversion materials. This has been reported by several authors, associating parallel-occurring processes, such as: (I) the increase in surface area in $Fe_3O_4$ nanoparticles-based electrodes during the first discharge, with the pristine oxide to the $Li_2O$/M composite formation[40]; (II) possible different reaction pathways during the conversion reaction.[41,42]

Rate capability tests for the $Fe_3O_4$/C composite using different current rate, ranging from 100 mA $g^{-1}$ to 2000 mA $g^{-1}$ are reported in Fig. 6 and detailed in Table I. The delivered capacity ranges from 984 mAh $g^{-1}$ at 100 mA $g^{-1}$ to 236 mAh $g^{-1}$ at 2000 mA $g^{-1}$, while, the ability to recover the original specific capacity is evaluated after 150 cycles at 250 $mAg^{-1}$. Average reversible capacity values of 660 $mAhg^{-1}$ were obtained, with a coulombic efficiency constantly exceeding 99.8%, see Table I. Specific capacity profiles of the rate capability test are shown in Fig. S4. At higher currents, the profiles become almost featureless, and this polarization effect could hint at a slower kinetic response of the conversion mechanism for stronger polarizations.

The good performance at high current rate and the outstanding electrochemical stability in the following 150 cycles at lower current rate, in which most of the original specific capacity is recovered, is due to different factors. First, the very small size of active material particles and the fibrous nature of the carbon material create a high conducting network favoring electronic transport. Secondly, the preparation procedure through ball milling of both the composite material and the electrode powder mix ensures a very close contact among the composite nanoparticles, the solid-state electrolyte and the conductive additive which benefit to the $Li^+$ diffusion and charge transfer kinetics.

Further extended galvanostatic cycling experiments were conducted using two high current-rate of at 500 mA $g^{-1}$ (current density 0.65 mA $cm^{-2}$) and 1000 mA $g^{-1}$ (current density 1.31 mA $cm^{-2}$) for over 1000 cycles, with the aim to check the prolonged stability of the solid-state cell, which are depicted in Fig. 7. In both experiments, the system shows an impressive cycling stability by reaching 1000 cycles mark without any failure. Considering the current rate of 500 mA $g^{-1}$, marked as (a) in the graph, the electrode highlights a capacity retention of 39.10% at the last cycle and an average capacity value of 240 $mAhg^{-1}$, while for the experiment at 1000 mA $g^{-1}$, marked as (b), the electrode has a capacity retention of 51.46% during the last cycle and an average capacity value of 193 mAh $g^{-1}$. It is to notice that the first cycles are crucial for a correct activation of the material. Indeed, in this initial phase of the experiment, it is concentrated most of the irreversible capacity loss, which is then followed by a stabilization over a high number of cycles. Figures S3 and S4 report details of the voltage profiles and differential analyses during these two experiments, which show

**Table I. Rate capability experiment specific capacity values at the different specific currents.**

| Specific Current/mA $g^{-1}$ | Current Density/mA $cm^{-2}$ | Capacity/mAh $g^{-1}$ |
|---|---|---|
| 100 | 0.13 | 984 |
| 200 | 0.26 | 777 |
| 500 | 0.65 | 606 |
| 1000 | 1.31 | 396 |
| 2000 | 2.62 | 236 |
| 250 | 0.32 | 662 (avg.) |

consistent electrochemical features with the rest of the electrochemical characterization.

Nyquist plots, in Fig. 8, have been acquired after full charge (3.000 V) by EIS measurements at selected cycle numbers (1, 5, 10, 50, 100, 200). All the EIS spectra are characterized by very large depressed semicircles in the medium frequency range, related to charge transfer processes (see in inset of Fig. 8), and a sloping line at low frequency related to diffusion processes. As a general trend, the overall impedance of the electrodes tends to a slight increase upon cycling. At the same time, an increase of impedance values upon cycling, mostly during the initial cycles, is a signal of a worsening of the charge-transfer kinetics, which may be related to partial nanoparticles re-aggregation, loss of electric contact, and interfacial degradation.

## Conclusions

$Fe_3O_4$ nanoparticles have been synthesized by a simple base-promoted method, and mechanically mixed with PAN derived electrospun carbon nanofibers. The characterization was performed using different techniques while the electrode powders have been prepared by ball milling of the composite material with $Li_3PS_4$-LiI sulfide solid-state electrolyte and conductive carbon additive.

Their electrochemical characterization revealed a very stable cycling performance showing features consistent with $Fe_3O_4$ conversion oxide and $Li_2S(Li_3PS_4)$ electrochemical mechanisms for a high number of galvanostatic cycles, with specific capacities of 506 mAh $g^{-1}$ after 350 cycles using 250 mA $g^{-1}$ current rate. Rate capability experiments showed very good performance with a remarkable capacity recovery during the long cycling at the end of the experiment. Prolonged cycling experiments at high current rate, 500 and 1000 mA $g^{-1}$ showed outstanding performance for over 1000 cycles. Preliminary electrochemical impedance spectroscopy experiments showed a quite stable interface. In conclusion, the use of all-solid-state cell configuration combined with the synthesis of inexpensive oxide like $Fe_3O_4$, easily synthesizable electrolyte and electrospun carbon fibers is very promising for the building of future LiBs with improved cycle-life and safety.

## Acknowledgments

This work was financially supported by Samsung SRJ, Minoh-Shi, Japan under a joint project supervised by Dr Aihara. M.A and A.M. acknowledge the support from the Chalmers Areas of Advance Materials Science and Energy, FORMAS, and the Swedish Energy Agency.

## ORCID

F. Maroni https://orcid.org/0000-0002-2534-5668
S. Brutti https://orcid.org/0000-0001-8853-9710
F. Croce https://orcid.org/0000-0001-9562-2694

## References

1. M. R. Palacín, *Chem. Soc. Rev.*, **38**, 2565 (2009).
2. M. N. Obrovac and V. L. Chevrier, *Chem. Rev.*, **114**, 11444 (2014).
3. J. Cabana, L. Monconduit, D. Larcher, and M. R. Palacín, *Adv. Mater.*, **22**, 170 (2010).
4. P. Poizot, S. Laruelle, S. Grugeon, and J.-M. Tarascon, *J. Electrochem. Soc.*, **149**, A1212 (2002).
5. S. Laruelle, S. Grugeon, P. Poizot, M. Dolle, L. Dupont, and J.-M. Tarascon, *J. Electrochem. Soc.*, **149**, A627 (2002).
6. N. Nitta, F. Wu, J. T. Lee, and G. Yushin, *Mater. Today*, **18**, 252 (2015).
7. Y. Oumellal, A. Rougier, G. A. Nazri, J.-M. Tarascon, and L. Aymard, *Nat. Mater.*, **7**, 916 (2008).
8. J. Hu, H. Li, and X. Huang, *Electrochem. Solid-State Lett.*, **8**, A66 (2005).
9. L. A. Montoro, J. M. Rosolen, J. H. Shin, and S. Passerini, *Electrochim. Acta*, **49**, 3419 (2004).
10. B. Das, M. V. Reddy, P. Malar, T. Osipowicz, G. V. Subba Rao, and B. V. R. Chowdari, *Solid State Ionics*, **180**, 1061 (2009).
11. D. C. S. Souza, V. Pralong, A. J. Jacobson, and L. F. Nazar, *Science*, **296**, 2012 (2002).
12. Y. Makimura, A. Rougier, L. Laffont, M. Womes, J. C. Jumas, J. B. Leriche, and J. M. Tarascon, *Electrochem. Commun.*, **8**, 1769 (2006).
13. L. Zhang, H. B. Wu, and X. W. Lou, *Adv. Energy Mater.*, **4**, 1 (2014).
14. Q. Q. Xiong, J. P. Tu, Y. Lu, J. Chen, Y. X. Yu, Y. Q. Qiao, X. L. Wang, and C. D. Gu, *J. Phys. Chem. C*, **116**, 6495 (2012).
15. A. Hu, X. Chen, Y. Tang, Q. Tang, L. Yang, and S. Zhang, *Electrochem. Commun.*, **28**, 139 (2013).
16. Y. Chen, H. Xia, L. Lu, and J. Xue, *J. Mater. Chem.*, **22**, 5006 (2012).
17. H. Wu, N. Du, J. Wang, H. Zhang, and D. Yang, *J. Power Sources*, **246**, 198 (2014).
18. J. S. Chen, Y. Zhang, and X. W. Lou, *ACS Appl. Mater. Interfaces*, **3**, 3276 (2011).
19. E. Kang, Y. S. Jung, A. S. Cavanagh, G. H. Kim, S. M. George, A. C. Dillon, J. K. Kim, and J. Lee, *Adv. Funct. Mater.*, **21**, 2430 (2011).
20. C. He, S. Wu, N. Zhao, C. Shi, E. Liu, M. Science, and F. Materials, *ACS Nano*, **7**, 4459 (2013).
21. G. Zhou, D. W. Wang, F. Li, L. Zhang, N. Li, Z. S. Wu, L. Wen, G. Q. Lu, and H. M. Cheng, *Chem. Mater.*, **22**, 5306 (2010).
22. L. Ji, Z. Tan, T. R. Kuykendall, S. Aloni, S. Xun, E. Lin, V. Battaglia, and Y. Zhang, *Phys. Chem. Chem. Phys.*, **13**, 7170 (2011).
23. J. Luo, J. Liu, Z. Zeng, C. F. Ng, L. Ma, H. Zhang, J. Lin, Z. Shen, and H. J. Fan, *Nano Lett.*, **13**, 6136 (2013).
24. F. Maroni, S. Gabrielli, A. Palmieri, E. Marcantoni, F. Croce, and F. Nobili, *J. Power Sources*, **332** (2016), 10.1016/j.jpowsour..09.1062016.
25. M. D. Abràmoff, P. J. Magalhães, and S. J. Ram, *Biophotonics Int.*, **11**, 36 (2004).
26. Maud Refinement Software Suite, http://maud.radiographema.eu/.
27. C. Haavik, S. Stølen, H. Fjellvåg, M. Hanfland, and D. Häusermann, *Am. Mineral.*, **85**, 514 (2000).
28. I. Slabu, N. Wirch, T. Caumanns, R. Theissmann, M. Krüger, T. Schmitz-Rode, and T. E. Weirich, *J. Phys. D: Appl. Phys.*, **50**, 315303 (2017).
29. W. Zhang, X. Li, R. Zou, H. Wu, H. Shi, S. Yu, and Y. Liu, *Sci. Rep.*, **5**, 11129 (2015).
30. X. Meng, Y. Xu, X. Sun, J. Wang, L. Xiong, X. Du, and S. Mao, *J. Mater. Chem. A*, **3**, 12938 (2015).
31. H. Xia, Y. Wan, G. Yuan, Y. Fu, and X. Wang, *J. Power Sources*, **241**, 486 (2013).
32. L. Yang, J. Hu, A. Dong, and D. Yang, *Electrochim. Acta*, **144**, 235 (2014).
33. H. Geng, Q. Zhou, Y. Pan, H. Gu, and J. Zheng, *Nanoscale*, **6**, 3889 (2014).
34. M. M. Thackeray, *J. Am. Ceram. Soc.*, **82**, 3347 (2004).
35. C. Ban, Z. Wu, D. T. Gillaspie, L. Chen, F. Yan, J. L. Blackburn, and A. C. Dillon, *Adv. Mater.*, **22**, 145 (2010).
36. S. H. Lee et al., *Nano Lett.*, **13**, 4249 (2013).
37. P. Lian, X. Zhu, H. Xiang, Z. Li, W. Yang, and H. Wang, *Electrochim. Acta*, **56**, 834 (2010).
38. M. Agostini, D. H. Lim, S. Brutti, N. Lindahl, J. H. Ahn, B. Scrosati, and A. Matic, *ACS Appl. Mater. Interfaces*, **10**, 34140 (2018).
39. T. Ohtomo, A. Hayashi, M. Tatsumisago, and K. Kawamoto, *Electrochemistry*, **81**, 428 (2013).
40. R. Alcántara, M. Jaraba, P. Lavela, J. L. Tirado, J. C. Jumas, and J. Olivier-Fourcade, *Electrochem. Commun.*, **5**, 16 (2003).
41. R. E. Doe, K. A. Persson, Y. S. Meng, and G. Ceder, *Chem. Mater.*, **20**, 5274 (2008).
42. N. Yamakawa, M. Jiang, B. Key, and C. P. Grey, *J. Am. Chem. Soc.*, **131**, 10525 (2009).